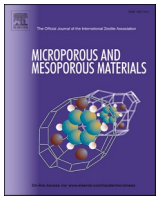
Microporous and Mesoporous Materials 376 (2024) 113188



Contents lists available at ScienceDirect

Microporous and Mesoporous Materials

journal homepage: www.elsevier.com/locate/micromeso





Investigating antimicrobial behavior of thymol/Zn encapsulated hierarchically structured zeolite and thymol release kinetics

Melda Isler Binay [a,*], Didem Kart [b], Burcu Akata [a,c]

[a] Department of Micro and Nanotechnology, Middle East Technical University, 06800, Ankara, Turkey
[b] Faculty of Pharmacy, Hacettepe University, 06100, Ankara, Turkey
[c] Central Laboratory, Middle East Technical University, 06800, Ankara, Turkey

ARTICLE INFO

Keywords:
Hierarchically zeolites
Thymol
Zinc
Release kinetics
Antimicrobial activity

ABSTRACT

A new bioactive material was proposed by encapsulating thymol molecules and Zn^{2+} cations within the post-modified intracrystalline voids of hierarchical zeolite X crystals. To enhance the accessibility of thymol molecules within zeolite X crystals, commercial zeolite samples underwent post-synthesis treatment involving consecutive aqueous KCl, NH_4Cl, and Na_2H_2EDTA solutions. The gas adsorption method utilized the encapsulation of both Zn^{2+} cation and thymol molecules into the resulting hierarchical zeolite X framework, which demonstrated improved antimicrobial activity. While sole thymol-encapsulated zeolite X exhibited no antimicrobial activity against *S. aureus*, Zn^{2+} encapsulated zeolite X (ZnX), thymol encapsulated post-treated zeolite X (HX-thy), and both Zn^{2+} and thymol encapsulated post-treated zeolite X (ZnHX-thy) displayed zone of inhibition values of 18.7 mm, 25.0 mm, and 37.5 mm, respectively. Adding Zn^{2+} and creating a hierarchical pore system in the zeolite X framework altered the release profiles. The Higuchi kinetic release model has the highest R^2 value to describe the process of thymol release from X-thy, whereas the Elovich release model has the best fitting profile of thymol release kinetics from ZnX-thy, HX-thy, and ZnHX-thy. Results indicate that thymol and Zn^{2+} containing hierarchical porous materials could be beneficial tools for obtaining enhanced antibacterial activity and stability with reduced degradation and volatility of thymol with extended protection against microbial attack due to the controlled release. These findings highlight an innovative approach to designing sustainable and green materials, utilizing modified porous networks that encapsulate natural antibacterial compounds with environmentally benign metal ions.

1. Introduction

Microbiological infection is becoming a serious concern. Hence, antimicrobial agents are created to limit the growth of microorganisms [1]. Plant-derived essential oils (EOs) such as thymol exhibit diverse industrial uses, and act as active components or additives in medicines and pharmaceuticals, owing to their distinctive physical-chemical and biological properties [2,3]. Thymol, known chemically as 2-isopropyl-5-methylphenol, is classified as a phenolic monoterpene. It is primarily found in various thyme species and constitutes a significant component of thyme essential oil. This aromatic compound is commonly sourced from the Mediterranean region [2]. Thymol possesses phenolic groups. Within these phenolic groups, hydroxyl groups play a crucial role in breaking down the outer membrane of gram-negative bacteria that contain lipopolysaccharides and proteins. This breakdown results in the leakage of lipopolysaccharides. The hydroxyl components also disrupt the plasma membrane, affecting the proton motive force (PMF) and electron flow [4,5].

EOs are gaining prominence across various applications due to their antimicrobial properties and their alignment with the trend toward a more sustainable and environmentally friendly lifestyle. However, the practical use of EOs is hindered by their natural tendency to degrade [6]. Encapsulating EOs within porous materials presents a viable solution, creating innovative essential oil delivery systems [7–10]. This encapsulation not only tackles the issue of EO volatility by protecting the molecules from degradation but also allows for controlled release, enhancing the efficacy and longevity of the EOs [10–12].

After extensive research, various techniques have been created to encapsulate bioactive components within nanoparticles or other nanocarriers. Within these nanocarriers, an appealing approach involves

* Corresponding author.
E-mail address: meldasler@gmail.com (M.I. Binay).

https://doi.org/10.1016/j.micromeso.2024.113188
Received 20 March 2024; Received in revised form 14 May 2024; Accepted 21 May 2024
Available online 23 May 2024
1387-1811/© 2024 Elsevier Inc. All rights are reserved, including those for text and data mining, AI training, and similar technologies.

encapsulating EO within microporous structures like aluminosilicates known as zeolites [11,13,14]. A considerable number of EO encapsulation methods for porous structures have been performed in the literature [7–9,11,13–16]. Nevertheless, the zeolite encapsulation methods for EOs are limited. Emulsification [13], solvent mixing [17–20], supercritical solvent impregnation [21], and gas adsorption [11,22] are the methodologies for the encapsulation of EOs into the zeolite framework. In addition, it should be noted that some studies integrate EOs into zeolite structures, but they lack evidence of the encapsulation of EOs, which is critical for the protection of EOs from environmental effects [13,23].

Additionally, it has been widely recognized that transition group metals, including silver, zinc, and copper, possess antibacterial properties. Unlike silver and copper, zinc (Zn^{2+}) is essential for microorganisms and complex organisms because it plays a crucial role in numerous vital biological processes at its low endogenous level [24]. Increasing Zn^{2+} concentrations above ideal levels disrupt Zn^{2+} homeostasis and let Zn^{2+} penetrate the cells, leading to toxicity in prokaryotes due to the elevated concentration [25]. As a result, Zn^{2+} may behave as an antibacterial and antifungal agent [26]. Over the past three decades, numerous studies have explored the utilization of zeolites, revealing that zeolites introduced with Zn^{2+} exhibit antibacterial effects in both synthetic and natural forms [27,28]. These zeolites, containing loaded Zn^{2+}, gradually release their properties, acting as inorganic bactericides and disinfectants [29]. Encapsulation of Zn^{2+} and EOs into zeolitic cages is particularly attractive for improved antimicrobial activity in a more sustainable lifestyle [14,30].

Furthermore, it was stated that surface modification of host material enhanced the adsorption of EOs and provided a more effective controlled release of EOs. By employing various surfactants and functionalizing agents, it is possible to customize the release characteristics within mesoporous compounds [31]. However, these procedures reduced the pore size in the host material, which decreases the capacity for loading molecules into the pores and the advantages of using a mesoporous host to encapsulate guest molecules. As an alternative approach, creating intra-crystalline mesopores can be employed to customize the adsorption and release behavior of EOs [11].

Zeolite X, featuring a pore size of 0.74 nm, has a significantly larger pore size compared to other zeolites and is one of the most widely manufactured zeolite types for use in adsorption processes in host-guest systems [32]. However, the size of the thymol molecule closely matches that of the zeolite X as indicated in Fig. 1. Therefore, this research aims to create hierarchical porosity in microporous zeolite X crystals by enlarging their pore sizes to more effectively encapsulate thymol molecules. The study presents a novel antimicrobial material that combines encapsulated Zn^{2+} cations with thymol molecules within hierarchical zeolite X. The research extensively explores the impact of induced enlargement on thymol loading and its release profiles within zeolite X. Additionally, the antibacterial properties of thymol-encapsulated zeolite X with the presence of Zn^{2+} were assessed, demonstrating its potential as a promising candidate for green and innovative antimicrobial solutions.

2. Materials and methods

Commercial zeolite X, thymol (≥98.5 %), and NaCl (ReagentPlus®, ≥99 %) were purchased from Sigma-Aldrich. KCl (99+%, ACS reagent) was received from ACROS Organics. $ZnSO_4.6H_2O$, NH_4Cl (for analysis EMSURE® ACS, ISO, Reag. Ph Eur), and Na_2H_2EDTA (Titriplex® III) were obtained from Merck. Phosphate buffer saline (PBS) was purchased from Chem-Lab. Deionized water is distilled from running tap water with a water purification system (Milli-Q system). All glassware was cleaned with deionized water and dried in an oven at 373 K. Materials for antimicrobial analyses were as follows. Mueller–Hinton and Saburaud dextrose agar (SDA) were purchased from Merck. Ciprofloxacin (≥98 %) and fluconazole (≥98 %) were obtained from Sigma-Aldrich. Blank sterile discs were purchased from Sigma-Aldrich for antimicrobial analysis. The schematic representation of the experimental process is demonstrated in Fig. 2.

2.1. Preparation of hierarchically structured zeolite X (HX)

Hierarchically structured zeolite X crystals were produced in three consecutive steps, as outlined in Table 1. The process is adapted from the study of Verboekend et al. [33]. All steps were performed with stirring. After each step, the formed crystals were cooled at room temperature, centrifuged, washed with deionized water three times, dried for a day at 323 K, and then used for the next step.

2.2. Ion exchange of X and HX (i.e. ZnX and ZnHX)

Preparation of $ZnSO_4{\cdot}6H_2O$ ion-exchange aqueous solutions was carried out for two distinct types of zeolite X: commercial and

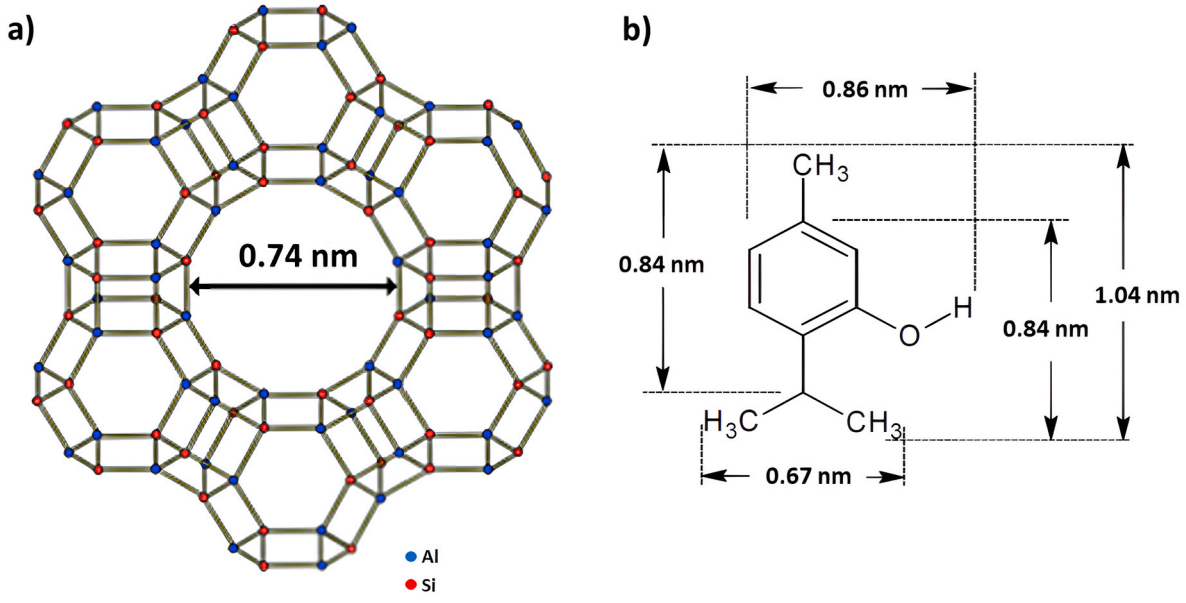


Fig. 1. Pore size of commercial zeolite X (a) (cations are not indicated.) [22] and structure of thymol (b) [7].

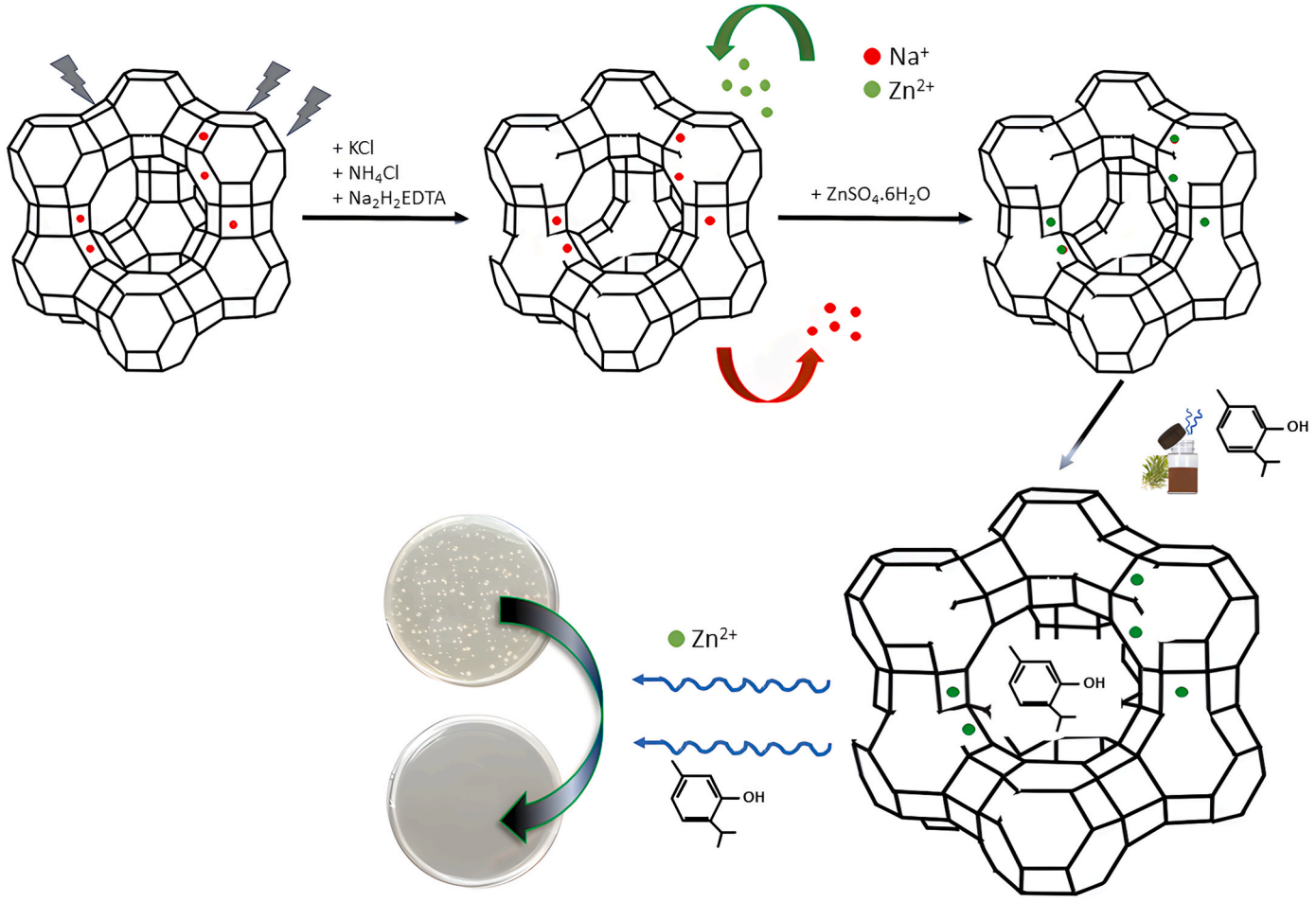


Fig. 2. Schematic representation of the experimental process.

Table 1
The list of chemical treatments for the production of hierarchically structured X.

# of steps	Chemical	Amount of zeolite (gr)	Volume of the solution (ml)	Concentration of the solution (M)	Time (h)	Temperature (°C)
1	KCl	10	130	3	2	65
2	NH_4Cl	10	500	3	2	65
3	Na_2H_2EDTA	1	62.5	0.11	6	100

hierarchically structured. The commercial zeolite X was immersed in a 0.032 M solution of $ZnSO_4{\cdot}6H_2O$, while the hierarchically structured zeolite was added to a 0.1 M solution. Both solutions were stirred vigorously for 24 h at room temperature.

2.3. Determination of thymol loading methodology

2.3.1. Methods of thymol loading into zeolites

Various methods were explored to encapsulate thymol into a zeolite framework based on the literature [7,22,23,34,35]. In the first approach, 0.5 g of thymol was dissolved in 10 ml of 70 wt% ethanol solution (ethanol/deionized water = 70/30). Subsequently, 1 g of zeolite X was introduced into the prepared thymol solution and stirred for 24 h at 40 °C. The resulting solution was washed with a 70 wt% ethanol solution (ethanol/deionized water = 70/30) and then centrifuged. The product obtained after drying at room temperature under vacuum was denoted as "M1-X-thy".

For the second method, referred to as "M2-X-thy", two separate solutions were prepared: thymol in ethanol (33.3 wt% thymol) for solution 1, and zeolite X in hot deionized water at 95 °C (33.3 wt% zeolite) for solution 2. These solutions were combined in the ratio of solution 1 to solution 2 = 5/1 and stirred at 50 °C for 30 min. The resulting blend was stirred at 25 °C for 24 h, followed by washing with 70 wt% ethanol solution (ethanol/deionized water = 70/30) three times, centrifugation, and drying at room temperature under vacuum.

In the third method, zeolite X crystals underwent a preliminary step of heating for 2 h at 220 °C to eliminate moisture. Subsequently, 0.5 g of zeolite X and 1 g of thymol were individually transferred into separate glass petri dishes. These petri dishes were then placed in a sealed glass vessel. They were left in the glass vessel for three months until the maximum loading level was reached. The resulting products from this method were labeled as "M3-X-thy". The schematic representation of the thymol loading methods is depicted in Fig. 3.

2.3.2. Comparison of thymol loading methods

The thymol concentration within the thymol-encapsulated zeolite X crystals was determined using an Agilent Cary 60 Diffuse reflectance UV–Vis spectrophotometer. The DR-UV-Vis spectra collected were further processed into absorption spectra using the Kubelka-Munk function $[(1\text{-}R)^2/2R]$, where R is the diffuse reflection of the sample.

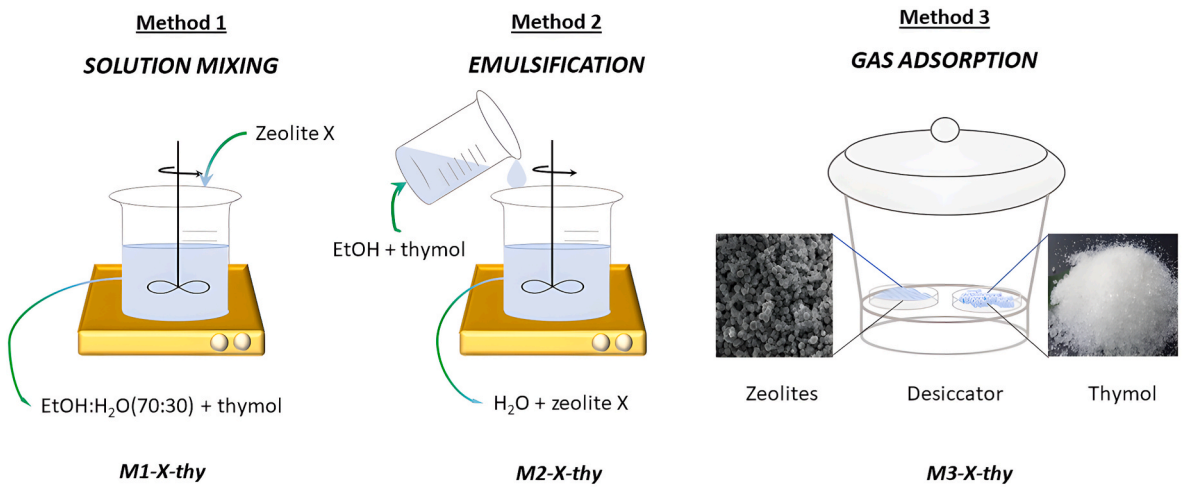


Fig. 3. Illustration of the thymol loading methods.

2.4. Thermal desorption study of thymol from hierarchically zeolite X

The thermal desorption study, as illustrated in Fig. S1, involved subjecting ZnHX-thy to pre-determined temperatures (i.e., 75 °C, 100 °C, 150 °C, 200 °C, 250 °C, and 300 °C) for fixed durations (i.e., 2 min, 5 min, and 7 min) (Fig. S1a). Subsequently, 0.05 g of ZnHX-thy from the oven was immersed in 20 ml of ethanol and stirred for 7 min (Fig. S1b). The solution was then centrifuged at 8000 rpm for 5 min (Fig. S1c). Following centrifugation, the supernatant was analyzed using a UV–Vis spectrophotometer (Fig. S1d). The supernatant contained the released thymol from the ZnHX-thy framework, and the thymol absorbance peak at 274 nm was recorded after UV–Vis spectrophotometer analysis. The released thymol from ZnHX-thy at room temperature served as the reference point (100 %). These procedures were repeated for each indicated time and temperature, and the thermal desorption graph was constructed with the recorded thymol absorbance peaks.

2.5. Release assay of thymol and kinetics

Thymol, released from the zeolite framework, was detected using the Agilent Cary 60 UV–Vis spectrophotometer at a wavelength of 274 nm. The release assays were performed in a 3.5 % w/v NaCl solution, prepared with phosphate-buffered saline (PBS), following the reported procedure [11]. The calibration curve of thymol at 274 nm, obtained and presented in Supplementary Information Fig. S2, was employed to calculate the concentration of the released thymol. To further study thymol release mechanisms from the hierarchical structures, various kinetic models were employed, including Higuchi [36], Korsmeyer-Peppas [37,38], Elovich [39], and first-order [12] as detailed in Eqs. (1)–(4):

$$\frac{M_t}{M_\infty} = k \times t^{1/2} \quad (1)$$

$$\frac{M_t}{M_\infty} = k \times t^n \quad (2)$$

$$M_t = k \times ln(t) \quad (3)$$

$$\ln M_t = ln\, M_0 - kt \quad (4)$$

$\frac{M_t}{M_\infty}$ is defined as the percent thymol released at time t, M_0 is the initial concentration of thymol in zeolite, and k corresponds to the release constant.

2.6. Antimicrobial assays

Disc diffusion tests were conducted against *P. aeruginosa* (ATCC 27853), *S. aureus* (ATCC 29213), and *C. albicans* (90028). Inoculums of bacteria and *C. albicans* yeast were dissolved in sterile saline and diluted according to the 0.5 McFarland standard. Subsequently, they were spread on Mueller–Hinton agar (Merck) and Saburaud dextrose agar (SDA) plates, respectively. The sample preparation was outlined in our previous work [11]. Suspensions of thymol-encapsulated zeolite crystals were prepared in 20 % wt/wt of ethanol. All organisms were inoculated on Mueller–Hinton agar and incubated at 37 °C overnight.

To test the antimicrobial activity of thymol-encapsulated zeolite crystals, paper discs with a diameter of 10 mm were loaded with 140 μL of the suspension and placed on agar plates. Following incubation for 24 h at 37 °C, the inhibition zones (mm) were determined. Ciprofloxacin (5 g) and fluconazole (25 g) were employed as standards [40,41]. All antimicrobial experiments were independently repeated three times (n = 3), and the mean inhibition zone value of the samples is presented as representative data in the current study.

2.7. Characterization

Commercial and hierarchically structured zeolite X morphologies were studied using a field-emission scanning electron microscope (Quanta 400F Field Emission SEM) and a high-resolution transmission electron microscope (HR-TEM) with JEOL JEM 2100F. X-ray powder diffraction (XRD) with a Rigaku-Ultima IV was used to identify the phase of commercial zeolite X, hierarchically structured zeolite X, and the Zn^{2+} exchanged forms of these zeolites. The diffraction peaks were scanned within the range of 5° and 50° with a speed of 1°/min. The Brunauer-Emmett-Teller (BET) method, conducted using Quantachrome Corporation's Autosorb-6, was employed to determine the total surface area and pore size distribution. The quantification of Zn^{2+} cations in the ion-exchanged zeolites was performed using inductively coupled plasma optical emission spectrometry (ICP-OES) with a PerkinElmer Optima 4300DV. An Agilent Technologies Cary 60 Diffuse reflectance UV–Vis spectrophotometer was utilized to measure thymol content.

3. Results and discussion

3.1. Characterization of zeolite X, hierarchically structured zeolite X, and ion-exchanged forms

The FE-SEM and HR-TEM images of the zeolite X and hierarchically structured zeolite X are given in Fig. 4. Fig. 4a and b reveal the typical

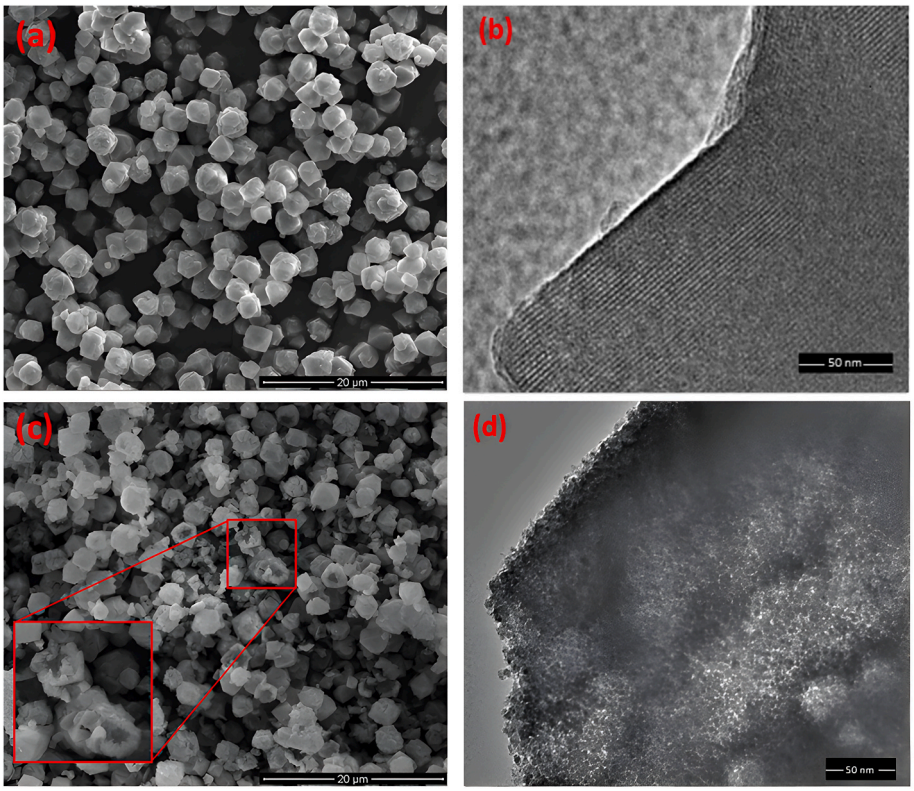


Fig. 4. SEM images of X (a) and HX (c), and TEM images of X (b) and HX (d).

intergrown crystal structure with well-crystalline morphology of commercial zeolite X respectively. According to Fig. 4c, the applied procedure changes the surface morphology with the occurrence of mesopores on the surface of the crystal (inset of Fig. 4c). Furthermore, the lattice fringes of the zeolite X disappear upon post-treatment, which indicates the loss of crystallinity with mesopore formation (Fig. 4d). This deformation can be due to the dealumination of the crystal structure, as also reported in the literature [33].

The pore structures of all samples were analyzed by N_2 adsorption-desorption isotherms, as depicted in Fig. 5. Both zeolite X and ZnX exhibited a typical type I isotherm indicative of a microporous structure, underscoring the preservation of microporous characteristic without subsequent post-synthesis treatment upon Zn^{2+} exchange. The post-synthesis treated samples, H-X and Zn-HX, exhibit type-IV isotherms with narrow and vertical hysteresis loops, signifying the emergence of mesoporosity. The porous structural parameters summarized in Table 2 also indicate an increase in the surface area from 644.5 to 838.3 m^2/g in HX upon post-treatment with a concurrent rise in the external surface area from 142.5 to 781.9 m^2/g. However, the micropore surface area showed a decrease from 502.2 to 56.4 m^2/g. Additionally, Zn loading in

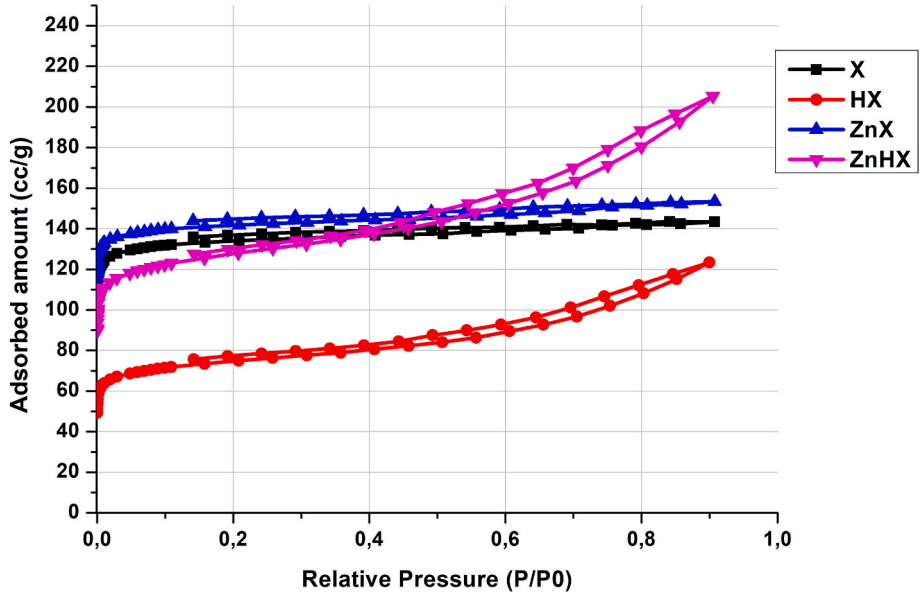


Fig. 5. Adsorption-desorption isotherms of X, HX, and ion-exchanged forms of these zeolites.

Table 2
Porous textural properties of the X and HX.

Sample Name	S_{BET} (m^2/g)[a]	S_{ext} (m^2/g)[b]	$S_{MicroPore}$ (m^2/g)[b]	Pore Volume (cc/g)[c]
X	644.5	142.2	502.2	0.26
HX	838.3	781.9	56.4	0.33

[a] Determined by Multipoint BET.
[b] Determined by t-Method.
[c] Determined by SF Method.

both commercial (ZnX) and hierarchically structured (ZnHX) zeolite X exhibited enhanced nitrogen uptake. This can be attributed to the replacement of two Na^+ cations with one divalent Zn^{2+} cation during the ion exchange process, leading to increased pore accessibility [42]. These findings suggest that the post-treatment applied to zeolite X samples, coupled with the ion exchange process, resulted in the formation of hierarchical pore formation, strategically aimed at facilitating higher thymol encapsulation.

The powder X-ray diffraction patterns of zeolite X, hierarchical zeolite X (HX), and their ion-exchanged forms are demonstrated in Fig. 6. Accordingly, the main peaks for zeolite X were also seen for all treated samples, indicating the structure was well preserved. However, the post-treatment approach led to a decrease in the peak intensity of zeolite X, particularly notable in the HX sample. Furthermore, subsequent ion exchange processes (ZnX and ZnHX) introduced a further reduction in crystallinity. The decline may be linked to the dealumination of the structure, potentially influenced by the positioning of extra-framework cations [43]. Following the ion exchange process, no additional diffraction peaks associated with Zn^{2+} cations were detected. The literature notes that such peaks typically appear at high concentrations, specifically around 20 % [44]. However, since the Zn^{2+} cation concentration in both ZnHX and ZnH is only 7 %, these additional peaks were not observed.

The ICP-OES analysis was conducted to elucidate the elemental composition of parent and post-modified samples and the results are shown in Table 3. The Si/Al ratio of zeolite X increased from 1.18 to 1.86 after the post-treated method (i.e., HX), indicating the dealumination of the zeolite framework upon applied treatment. As indicated in Table 3, the Na^+ concentration decreased upon the loading of Zn^{2+}, suggesting a successful ion-exchange of Zn^{2+} with Na^+ ions. Subsequently, thymol was encapsulated into ZnX and ZnHX samples and the maximum loading of Zn^{2+} was determined as 7.2 wt% for ZnHX. To maintain thymol concentration as the sole variable in this study, the Zn^{2+} concentration in ZnX was adjusted to be about 7 wt%.

Table 3
ICP-OES results of the X, TX, and ion-exchanged forms of these zeolites.

Sample	Si/Al ratio	Na wt.%	Zn wt.%
X	1.18 ± 0.2	9.1 ± 0.3	–
HX	1.86 ± 0.2	6.0 ± 0.3	–
ZnX	1.18 ± 0.2	5.2 ± 0.2	6.8 ± 0.2
ZnHX	1.86 ± 0.2	1.9 ± 0.1	7.2 ± 0.2

3.2. Thymol loading into zeolites

Fig. 7 illustrates various methods used to encapsulate thymol into the zeolite X framework. The method resulting in the maximum intensity at 274 nm, which represents the characteristic UV–Vis peak of thymol molecules, was selected for the encapsulation method. The gas adsorption method, M3-X-thy, was found to be the most effective by achieving the highest quantity of encapsulation quantity without requiring additional solvents. This method outperformed traditional methods documented in the literature (i.e., M1-X-thy, M2-X-thy), such as solvent mixing [17–20], and emulsification [13].and emulsification. Therefore, the gas adsorption method, M3-X-thy, was selected for all subsequent studies.

The percent encapsulation of thymol for each sample was calculated using Eq. (5);

$$\%\ Encapsulation\ of\ thymol = \frac{weight\ of\ thymol\ (m_{THY})}{weight\ of\ zeolite\ (m_Z)} \quad (5)$$

where m_Z is the weight of zeolite X at the end of the encapsulation process and m_{THY} is the weight difference of zeolite crystals before and after placement in the desiccator.

Fig. 8a displays the thymol encapsulation percentage, indicating the amount of thymol encapsulated into respective zeolites. The thymol encapsulation percent (% wt/wt) were calculated as 0.41 ± 0.06, 0.44 ± 0.06, 6.77 ± 0.59, and 7.82 ± 0.44 for X-thy, ZnX-thy, HX-thy, and ZnHX-thy, respectively. These results suggest that the post-treatment method applied to the hierarchical pore structure successfully enhanced thymol loading into zeolite X.

3.3. Thermal desorption study of thymol from hierarchically zeolite X

In the literature, Thermal Gravimetric analyses were performed to assess the thermal stability of samples. However, it is crucial to note that the thymol amount in X-thy and ZnX-thy fell below the detection limit, while in HX and ZnHX, it was very close to the detection limit in this

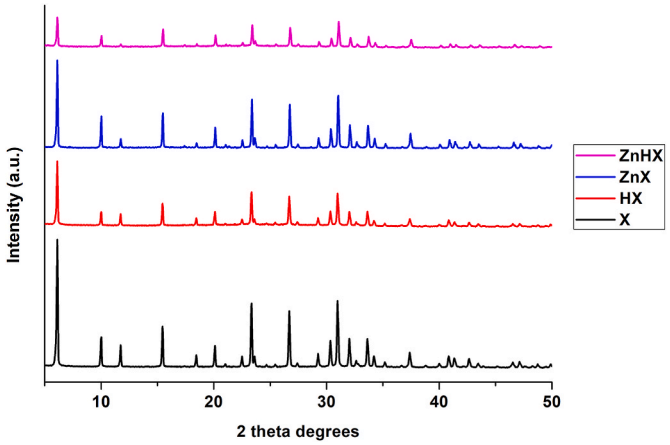


Fig. 6. XRD patterns of X, HX, and ion-exchanged forms of these zeolites.

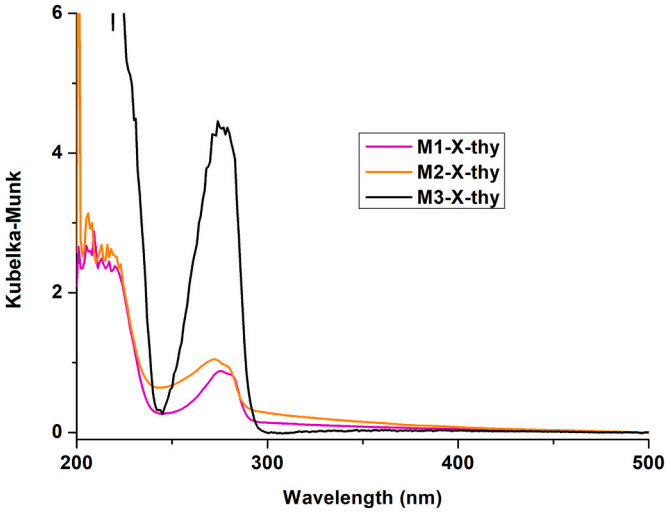


Fig. 7. Thymol loading based on the different methods.

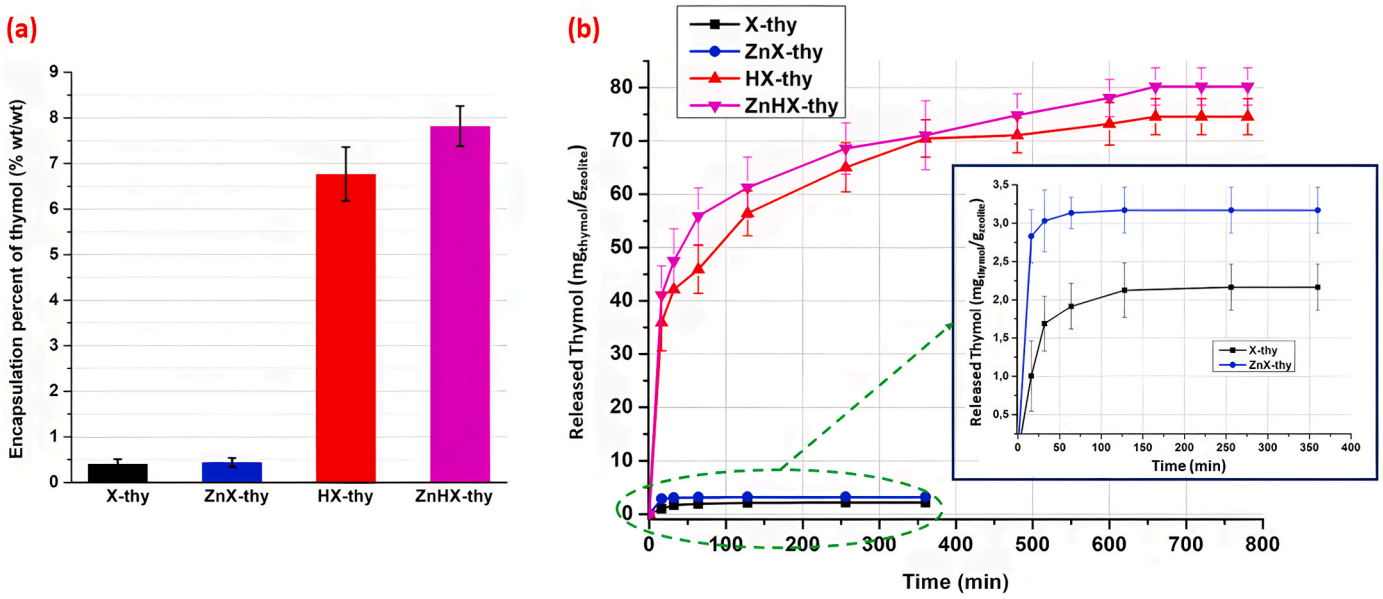


Fig. 8. Encapsulation percent of thymol (a) and the thymol release from X-thy and ZnX-thy and HX-thy and ZnHX-thy (b).

study. As a result, an alternative method focusing on the thermal desorption of thymol from ZnHX-thy was explored specifically focusing on the thermal stability of this particular sample and providing further insides into its behavior upon thymol encapsulation.

Fig. 9 illustrates the variation in the amount of thymol in ZnHX-thy (% w/w) with different durations and temperatures of exposure in the oven. The percentage of thymol in ZnHX-thy pattern can be categorized into three regions. The most significant decrease was observed in Region-I, followed by Region-III.

As depicted in Fig. 9, the percentage of thymol in ZnHX-thy decreased with the increase in temperature, maintained for all durations (2-5-7 min). It was seen that the thymol percentage after the treatment at 300 °C decreased with the duration of exposure, with percentages of 31 and 11 % for 2 and 5 min, respectively. Extending the exposure to 7 min releases all available thymol molecules, whereas residual thymol was still present in the pores after 2 and 5 min at 300 °C. The thermal gravimetric analysis (TGA) of thymol, shown in the inset graph in Fig. 9, exhibits the evaporation of all thymol molecules completed at 200 °C. It supports the proposition that the process using zeolite X effectively encapsulates the thymol molecule, resulting in its release at higher temperatures. This effect is particularly evident in Region-II for temperatures between 100 °C and 250 °C. Following a sharp decrease in thymol percentage observed up to 100 °C, the amount of thymol desorbed from the samples exhibited a more linear profile for 5 and 7 min of exposure. For samples exposed for 5 min at 250 °C, approximately 40 % thymol remained in ZnHX-thy. It appears that the physisorbed amount desorbed from the outer surface up to 100 °C, while the extended desorption of thymol from the inner framework occurs at higher temperatures. This behavior suggests that the developed encapsulation method successfully enhanced thermal stability and promoted prolonged release at higher temperatures.

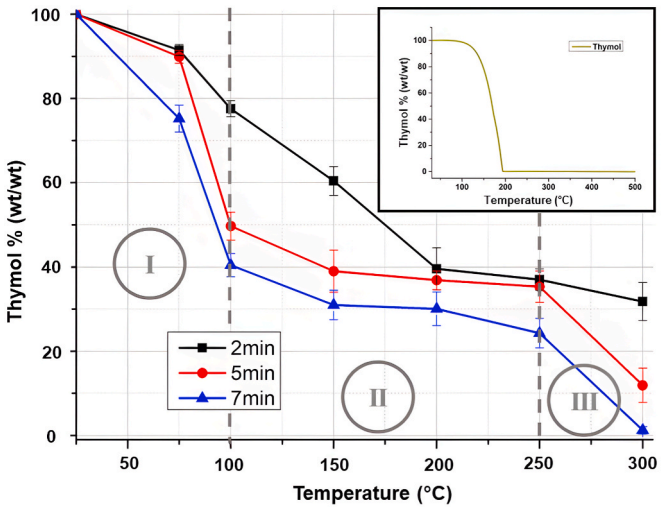


Fig. 9. Thermal desorption study of thymol from ZnHX-thy framework.

3.4. Release assay of thymol and kinetics

The in vitro release of thymol in the solution of PBS with 3.5 % wt NaCl is presented in Fig. 8b. The study revealed that X-thy released 2.2 ± 0.5 mg g^{-1} of thymol in 260 min, while ZnX-thy released a slightly higher amount of thymol (3.1 ± 0.2 mg g^{-1}) in a shorter time (70 min). This observation may be attributed to the replacement of two Na^{+} ions with one divalent Zn^{2+} cation, leading to an increase in pore accessibility for thymol molecules [42]. Both HX-thy and ZnHX-thy exhibited a significant increase in the amount of released thymol, with a slightly higher release for ZnHX-thy due to superior adsorption of thymol molecules. The release of thymol amounts was found to be 74.3 ± 3.3 and 80.4 ± 3.5 mg g^{-1} for HX-thy and ZnHX-thy, respectively. Furthermore, the release process was completed at 660 min for both samples. The significant increase in the amount released can be due to the hierarchical structure created in zeolite X upon applying the post-treatment process. A kinetic model was developed to provide a detailed assessment of the release mechanism for these samples.

Several kinetic models for released thymol from zeolite X samples were assessed. The calculated release rate (k) for the different models and the coefficient of determination (R^2) are presented in Table 4. The most suitable model to describe the release mechanism of thymol from X-thy is the Higuchi kinetic release model with the highest R^2 value (R^2 = 0.9727). In this release model, the cumulative amount of drug released is directly proportional to the square root of time. The Higuchi kinetic release model is based on Fickian diffusion [45]. This model is a mathematical equation that explains the release rate of drugs from a solid matrix structure and is suitable for the systems in which the guest is homogeneously dispersed in the host materials [46].

Table 4
The release kinetics models of thymol from zeolite X samples.

Release Kinetics Model		X-thy	ZnX-thy	TX-thy	ZnTX-thy
Higuchi	k	11.627	82.587	50.539	69.827
	R^2	0.9727	0.65	0.858	0.8769
Korsemeyer-Peppas	k	11.501	1.002	0.1509	0.9461
	R^2	0.9546	0.8414	0.8856	0.8906
Zero order	k	0.6147	12.915	0.8447	0.4868
	R^2	0.7985	0.5383	0.6459	0.605
Elovich	k	19.149	21.815	15.612	16.859
	R^2	0.9695	0.8819	0.9933	0.9940

The data presented in Table 4 indicates that the ion-exchange and post-treatment processes had a significant effect on the thymol release kinetics from the zeolite structure. Specifically, the ion-exchange process resulted in a rapid release of thymol, as shown in Fig. 8b. Even if the best appropriate kinetic release model seems to be the Elovich kinetic release model according to Table 4, the coefficient of determination is quite low (i.e., $R^2 = 0.8819$) for ZnX-thy.

After the post-treatment process, the best fitting profile of the thymol release kinetics from HX-thy was determined to be the Elovich release model with a high coefficient of determination (i.e., $R^2 = 0.9933$), as demonstrated in Table 4. For the release of thymol from ZnHX-thy, the R^2 value is close to HX-thy (i.e., $R^2 = 0.9940$). Additionally, similar release behavior is displayed in Fig. 8b. Thus, the Elovich release model was found to be the most proper release model for the release of thymol from ZnHX-thy, as noted in Table 4. The thymol release occurs through a logarithmic and time-dependent transport mechanism in the Elovich release profile. This profile delineates the rapid release of adsorbed thymol on the host's outer surface and the slow release of thymol placed in the inner parts of the host [39]. The post-treatment process can be suggested to improve the accessibility of the zeolite X's surface area and increase the amount of adsorbed thymol. Accordingly, it can be postulated that the superior release of thymol encapsulated from zeolite HX samples exhibited a unique thymol release profile concerning their counterparts.

3.5. Antimicrobial assays

The antimicrobial assays of thymol-loaded zeolite X were assessed against *P. aeruginosa* as a gram-negative bacterium, *S. aureus* as a gram-positive bacterium, and *C. albicans* as a yeast. The disc diffusion assays' results are graphically illustrated in Fig. 10. The detailed results are shown in Figs. S4–S6 and listed in Table S1.

As per the results depicted in Fig. 10, neither X nor HX exhibited any antimicrobial activity against any of the three microorganisms tested. However, the ion-exchange of Zn^{2+} cations within the zeolite framework resulted in antimicrobial activity, as evidenced by ZnX and ZnHX. The higher antimicrobial efficacy of ZnX toward *S. aureus* among all microorganisms is attributed to the low concentration of Zn^{2+} ions within the framework. Consistent with findings in the literature, ZnX exhibited activity against *S. aureus* but not against *P. aeruginoda* and *C. albicans* [47]. Notably, ZnHX displayed zones of inhibition measuring 22.0 mm, 13.7 mm, and 19.0 mm against *S. aureus, P. aeruginosa,* and *C. albicans,* respectively, whereas HX exhibited no antimicrobial activity.

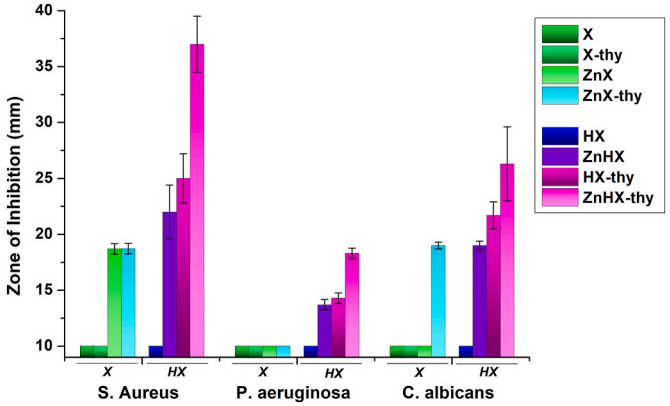


Fig. 10. Results of disc diffusion assays for zeolite X samples.

While the literature asserts that thymol molecules possess antimicrobial activity against a broad spectrum of microorganisms, it was observed that X-thy did not exhibit any antimicrobial effect [48]. This absence of activity could be attributed to the inadequate adsorption of thymol within the zeolite X crystals, resulting in insufficient antimicrobial activity. However, following a post-treatment process aimed at enlarging the pore structure, a significant enhancement in antimicrobial activity was achieved due to higher thymol adsorption. Consequently, HX-thy demonstrated remarkable antimicrobial activity against all microorganisms tested with inhibition zones measuring 25.0 mm, 14.3 mm, and 21.7 mm *S. aureus, P. aeruginosa,* and *C. albicans,* respectively.

Additionally, the incorporation of Zn^{2+} cations into the framework resulted in increased antimicrobial activity within the zeolite structure (ZnHX-thy) compared to samples lacking additional cations (HX-thy). This unique zeolitic system (i.e., ZnHX-thy) exhibited inhibition zones measuring 37.5 mm, 18.7 mm, and 26.3 mm against *S. aureus, P. aeruginosa,* and *C. albicans,* respectively. The combination of zinc and EOs presented a synergistic effect in enhancing antimicrobial activity [49–51]. This phenomenon is likely attributable to the capacity of EOs to sensitize bacterial cells, thereby diminishing their resistance to zinc. This effect likely involves EOs altering cellular mechanisms, such as modulating the concentration of adenosine triphosphate and/or the hyperpolarization of the cell wall. These changes lead to lowered cytoplasmic pH, which in turn facilitates the binding of zinc ions to proteins and enzymes thereby disrupting critical cellular functions [49].

In summary, the implementation of the post-treatment process, designed to create enlarged microporosity through combined ion-exchange and thymol encapsulation, has led to exceptional antimicrobial activity for all microorganisms. It is worth to note that notably this potent antibacterial activity was achieved utilizing zeolites integrated with a relatively low concentration of thymol (i.e. 7.82 %) compared to the literature [16,23]. It is crucial to highlight that such efficacy was not observed in counterparts treated solely with Zn^{2+}/thymol (ZnHX or HX-thy) or untreated samples (ZnX or HX). This underscores that neither post-treatment nor ion exchange processes exhibited significant antimicrobial activity. Instead, it is the synergistic effect of combining these processes that resulted in enhanced activity observed throughout this study.

4. Conclusions

This study demonstrates the effectiveness of a strategic approach that combines Zn^{2+} exchange with a post-treatment process creating hierarchical porosity in zeolites to enhance antimicrobial activity alongside thymol adsorption. To obtain this novel antimicrobial host-guest system, zeolite X was sequentially treated with the aqueous solutions of KCl, NH_4Cl, and Na_2H_2EDTA for the controlled dealumination of the structure, which offered higher accessibility of surface area for thymol molecules and controlled release of thymol. Subsequent Zn^{2+} exchange and thymol encapsulation were executed with flair. The resulting hierarchical material, incorporating Zn^{2+} exchange and thymol-loaded features, exhibited superior antimicrobial activity compared to its counterparts. This underscores the importance of integrating the post-treatment process, Zn^{2+} exchange, and thymol encapsulation within the zeolitic frameworks.

CRediT authorship contribution statement

Melda Isler Binay: Writing – review & editing, Writing – original

draft, Visualization, Validation, Methodology, Investigation, Formal analysis, Data curation, Conceptualization. **Didem Kart:** Resources, Investigation. **Burcu Akata:** Writing – review & editing, Supervision, Resources, Project administration, Funding acquisition, Conceptualization.

Declaration of competing interest

The authors declare that they have no known competing financial interests or personal relationships that could have appeared to influence the work reported in this paper.

Data availability

Data will be made available on request.

Acknowledgments

No funding was received to assist with this research. The support provided by METU-Central Laboratory is greatly acknowledged.

Appendix A. Supplementary data

Supplementary data to this article can be found online at https://doi.org/10.1016/j.micromeso.2024.113188.

References

[1] K. Malachova, P. Praus, Z. Rybkova, O. Kozak, Antibacterial and antifungal activities of silver, copper and zinc montmorillonites, Appl. Clay Sci. 53 (2011) 642–645, https://doi.org/10.1016/j.clay.2011.05.016.
[2] A. Kowalczyk, M. Przychodna, S. Sopata, A. Bodalska, I. Fecka, Thymol and thyme essential oil—new insights into selected therapeutic applications, Molecules 25 (2020) 4125–4142, https://doi.org/10.3390/molecules25184125.
[3] X. Xu, K. Song, J. Guo, S. Liu, X. Zhou, J. He, Adsorption behavior of amino functionalized MCM-41 on chlorogenic acid from Eucommia ulmoides leaves, J. Porous Mater. 30 (2023) 71–81, https://doi.org/10.1007/s10934-022-01323-0.
[4] I.M. Helander, H.-L. Alakomi, K. Latva-Kala, T. Mattila-Sandholm, I. Pol, E.J. Smid, L.G.M. Gorris, A. von Wright, Characterization of the action of selected essential oil components on gram-negative bacteria, J. Agric. Food Chem. 46 (1998) 3590–3595, https://doi.org/10.1021/jf980154m.
[5] H.J. Dorman, S.G. Deans, Antimicrobial agents from plants: antibacterial activity of plant volatile oils, J. Appl. Microbiol. 88 (2000) 308–316, https://doi.org/10.1046/j.1365-2672.2000.00969.x.
[6] A.P. Ferreira, C. Almeida-Aguiar, S.P.G. Costa, I.C. Neves, Essential oils encapsulated in zeolite structures as delivery systems (EODS): an overview, Molecules 27 (2022) 1–24, https://doi.org/10.3390/molecules27238525.
[7] X.H. Chai, R.H. Lin, K.G. Wu, S.R. Li, Characterization of β-cyclodextrin-thymol inclusion complexes, Adv. Mater. Res. 233–235 (2011) 1766–1773, https://doi.org/10.4028/www.scientific.net/AMR.233-235.1766.
[8] P.A. Ponce Cevallos, M.P. Buera, B.E. Elizalde, Encapsulation of cinnamon and thyme essential oils components (cinnamaldehyde and thymol) in β-cyclodextrin: effect of interactions with water on complex stability, J. Food Eng. 99 (2010) 70–75, https://doi.org/10.1016/j.jfoodeng.2010.01.039.
[9] R. Zhang, Y. Cui, M. Cheng, Y. Guo, X. Wang, J. Wang, Antifungal activity and mechanism of cinnamon essential oil loaded into mesoporous silica nanoparticles, Ind. Crop. Prod. 171 (2021) 113846, https://doi.org/10.1016/j.indcrop.2021.113846.
[10] J.N. Saucedo-Zuñiga, S. Sánchez-Valdes, E. Ramírez-Vargas, L. Guillen, L.F. Ramos-deValle, A. Graciano-Verdugo, J.A. Uribe-Calderón, M. Valera-Zaragoza, T. Lozano-Ramírez, J.A. Rodríguez-González, J.J. Borjas-Ramos, J.D. Zuluaga-Parra, Controlled release of essential oils using laminar nanoclay and porous halloysite/essential oil composites in a multilayer film reservoir, Microporous Mesoporous Mater. 316 (2021), https://doi.org/10.1016/j.micromeso.2021.110882.
[11] M.I. Binay, D. Kart, B. Akata, Enhanced antimicrobial activity of volatile thymol molecules encapsulated in hierarchical titanosilicates, J. Porous Mater. 30 (2023) 619–628, https://doi.org/10.1007/s10934-022-01367-2.
[12] M. Sotelo-Boyás, Z. Correa-Pacheco, S. Bautista-Baños, Y. Gómez y Gómez, Release study and inhibitory activity of thyme essential oil-loaded chitosan nanoparticles and nanocapsules against foodborne bacteria, Int. J. Biol. Macromol. 103 (2017) 409–414, https://doi.org/10.1016/j.ijbiomac.2017.05.063.
[13] Z. Milićević, S. Krnjajić, M. Stević, J. Ćirković, A. Jelušić, M. Pucarević, T. Popović, Encapsulated clove bud essential oil: a new perspective as an eco-friendly biopesticide, Agric. For. 12 (2022) 1–13, https://doi.org/10.3390/agriculture12030338.
[14] R. Tekin, N. Bac, Antimicrobial behavior of ion-exchanged zeolite X containing fragrance, Microporous Mesoporous Mater. 234 (2016) 55–60, https://doi.org/10.1016/j.micromeso.2016.07.006.
[15] Z. Xiao, H. Bao, S. Jia, Y. Bao, Y. Niu, X. Kou, Organic hollow mesoporous silica as a promising sandalwood essential oil carrier, Molecules 26 (2021) 2744.
[16] K. Sharma, M. Munjal, R.K. Sharma, M. Sharma, Thymol encapsulated chitosan-Aloe vera films for antimicrobial infection, Int. J. Biol. Macromol. 235 (2023) 123897, https://doi.org/10.1016/j.ijbiomac.2023.123897.
[17] A. Ebadollahi, J.J. Sendi, W.N. Setzer, T. Changbunjong, Encapsulation of Eucalyptus largiflorens essential oil by mesoporous silicates for effective control of the cowpea weevil, callosobruchus maculatus (fabricius) (Coleoptera: chrysomelidae), Molecules 27 (2022) 3531, https://doi.org/10.3390/molecules27113531.
[18] M. Mojarab-mahboubkar, Z. Afrazeh, R. Azizi, J.J. Sendi, Efficiency of Artemisia annua L . essential oil and its chitosan/tripolyphosphate or zeolite encapsulated form in controlling Sitophilus, Pestic. Biochem. Physiol. 195 (2023) 105544, https://doi.org/10.1016/j.pestbp.2023.105544.
[19] S.P.G. Costa, O.S.G.P. Soares, C.A. Aguiar, I.C. Neves, Fragrance carriers obtained by encapsulation of volatile aromas into zeolite structures, Ind. Crop. Prod. 187 (2022) 115397, https://doi.org/10.1016/j.indcrop.2022.115397.
[20] J. Zuniega, J. Grabulos, M. Lebrun, T. Aumond, C. Daniel, P. Brat, D. Farrusseng, Encapsulation of thymol and limonene in metal – organic frameworks for inhibition of Colletotrichum musae growth, Int. J. Food Sci. Technol. 59 (2024) 730–742, https://doi.org/10.1111/ijfs.16812.
[21] J. Dikić, I. Lukić, J. Pajnik, J. Pavlović, J. Hrenović, N. Rajić, Antibacterial activity of thymol/carvacrol and clinoptilolite composites prepared by supercritical solvent impregnation, J. Porous Mater. 28 (2021) 1577–1584, https://doi.org/10.1007/s10934-021-01107-y.
[22] R. Tekin, N. Bac, J. Warzywoda, A. Sacco, Encapsulation of a fragrance molecule in zeolite X, Microporous Mesoporous Mater. 215 (2015) 51–57, https://doi.org/10.1016/j.micromeso.2015.05.020.
[23] S. Cometa, M.A. Bonifacio, A. Bellissimo, L. Pinto, A. Petrella, N. De Vietro, G. Iannaccone, F. Baruzzi, E. De Giglio, A green approach to develop zeolite-thymol antimicrobial composites: analytical characterization and antimicrobial activity evaluation, Heliyon 8 (2022) e09551, https://doi.org/10.1016/j.heliyon.2022.e09551.
[24] H. Haase, S. Overbeck, L. Rink, Zinc supplementation for the treatment or prevention of disease: current status and future perspectives, Exp. Gerontol. 43 (2008) 394–408, https://doi.org/10.1016/j.exger.2007.12.002.
[25] B. Sugarman, Zinc and infection, Rev. Infect. Dis. 5 (1983) 137–147, https://doi.org/10.1093/clinids/5.1.137.
[26] N. Mutlu, L. Liverani, F. Kurtuldu, D. Galusek, A.R. Boccaccini, Zinc improves antibacterial, anti-inflammatory and cell motility activity of chitosan for wound healing applications, Int. J. Biol. Macromol. 213 (2022) 845–857, https://doi.org/10.1016/j.ijbiomac.2022.05.199.
[27] A. Top, S. Ülkü, Silver, zinc, and copper exchange in a Na-clinoptilolite and resulting effect on antibacterial activity, Appl. Clay Sci. 27 (2004) 13–19, https://doi.org/10.1016/j.clay.2003.12.002.
[28] P. Kaali, G. Czél, Single, Binary and Ternary Ion-Exchanged Zeolite as an Effective Bioactive Filler for Biomedical Polymer Composites, vol. 729, 2013, pp. 99–104, https://doi.org/10.4028/www.scientific.net/MSF.729.234.
[29] H. Jia, W. Hou, L. Wei, B. Xu, X. Liu, The structures and antibacterial properties of nano-SiO2 supported silver/zinc-silver materials, Dent. Mater. 24 (2008) 244–249, https://doi.org/10.1016/j.dental.2007.04.015.
[30] B. Niu, Z. Yan, P. Shao, J. Kang, H. Chen, Encapsulation of cinnamon essential oil for active food packaging film with synergistic antimicrobial activity, Nanomaterials 8 (2018), https://doi.org/10.3390/nano8080598.
[31] A. Jobdeedamrong, R. Jenjob, D. Crespy, Encapsulation and release of essential oils in functional silica nanocontainers, Langmuir 34 (2018) 13235–13243, https://doi.org/10.1021/acs.langmuir.8b01652.
[32] K. Weh, M. Noack, I. Sieber, J. Caro, Permeation of single gases and gas mixtures through faujasite-type molecular sieve membranes, Microporous Mesoporous Mater. 54 (2002) 27–36, https://doi.org/10.1016/S1387-1811(02)00381-5.
[33] D. Verboekend, T.C. Keller, S. Mitchell, J. Pérez-Ramírez, Hierarchical FAU- and LTA-type zeolites by post-synthetic design: a new generation of highly efficient base catalysts, Adv. Funct. Mater. 23 (2013) 1923–1934, https://doi.org/10.1002/adfm.201202320.
[34] A. Rukmani, M. Sundrarajan, Inclusion of antibacterial agent thymol on -cyclodextrin-grafted organic cotton, J. Ind. Text. 42 (2011) 132–144, https://doi.org/10.1177/1528083711430244.
[35] M. Shahriarinour, F. Divsar, Z. Eskandari, Synthesis, characterization, and antibacterial activity of thymol loaded SBA-15 mesoporous silica nanoparticles, Inorg. Nano-Metal Chem. 49 (2019) 182–189, https://doi.org/10.1080/24701556.2019.1624569.
[36] H. Rezaeinia, B. Ghorani, B. Emadzadeh, M. Mohebbi, Prolonged-release of menthol through a superhydrophilic multilayered structure of balangu (Lallemantia royleana)-gelatin nanofibers, Mater. Sci. Eng. C 115 (2020) 111115, https://doi.org/10.1016/j.msec.2020.111115.
[37] I.Y. Wu, S. Bala, N. Škalko-Basnet, M.P. di Cagno, Interpreting non-linear drug diffusion data: utilizing Korsmeyer-Peppas model to study drug release from liposomes, Eur. J. Pharmaceut. Sci. 138 (2019) 105026, https://doi.org/10.1016/j.ejps.2019.105026.
[38] Y. Chen, A. Mensah, Q. Wang, D. Li, Y. Qiu, Q. Wei, Hierarchical porous nanofibers containing thymol/beta-cyclodextrin: physico-chemical characterization and potential biomedical applications, Mater. Sci. Eng. C 115 (2020) 111155, https://doi.org/10.1016/j.msec.2020.111155.

[39] B.D. Mattos, B.L. Tardy, M. Pezhman, T. Kämäräinen, M. Linder, W.H. Schreiner, W.L.E. Magalhães, O.J. Rojas, Controlled biocide release from hierarchically-structured biogenic silica: surface chemistry to tune release rate and responsiveness, Sci. Rep. 8 (2018) 1–11, https://doi.org/10.1038/s41598-018-23921-2.

[40] N. Rangkadilok, S. Tongchusak, R. Boonhok, S.C. Chaiyaroj, V.B. Junyaprasert, W. Buajeeb, J. Akanimanee, T. Raksasuk, T. Suddhasthira, J. Satayavivad, In vitro antifungal activities of longan (Dimocarpus longan Lour.) seed extract, Fitoterapia 83 (2012) 545–553, https://doi.org/10.1016/j.fitote.2011.12.023.

[41] K. Bush, M.N. Dudley, Performance Standards for Antimicrobial Disk Susceptibility Tests ; Approved Standard — Tenth Edition, 2009.

[42] M. Ben Abda, O. Schäf, Y. Zerega, Ion exchange effect on asymmetric dioxins adsorption onto FAU-type X-zeolites, Microporous Mesoporous Mater. 217 (2015) 178–183, https://doi.org/10.1016/j.micromeso.2015.06.013.

[43] M.L.M. Oliveira, A.A.L. Miranda, C.M.B.M. Barbosa, C.L. Cavalcante, D.C. S. Azevedo, E. Rodriguez-Castellon, Adsorption of thiophene and toluene on NaY zeolites exchanged with Ag(I), Ni(II) and Zn(II), Fuel 88 (2009) 1885–1892, https://doi.org/10.1016/j.fuel.2009.04.011.

[44] U. Steinike, K. Jancke, W. Lutz, E. Schreier, G. Walther, NaA-zeolites modified by me^{2+}-cations, Mater. Sci. Forum 228–231 (1996) 669–676, https://doi.org/10.4028/www.scientific.net/MSF.228-231.669.

[45] M.P. Paarakh, P.A.N.I. Jose, C.M. Setty, G. V Peter, Release kinetics – concepts and applications, Int. J. Pharm. Res. Technol. 8 (2019) 12–20, https://doi.org/10.31838/ijprt/08.01.02.

[46] D. Tan, P. Yuan, F. Annabi-Bergaya, D. Liu, L. Wang, H. Liu, H. He, Loading and in vitro release of ibuprofen in tubular halloysite, Appl. Clay Sci. 96 (2014) 50–55, https://doi.org/10.1016/j.clay.2014.01.018.

[47] S. Demirci, Z. Ustaoglu, G.A. Yilmazer, F. Sahin, N. Bac, Antimicrobial properties of zeolite-X and zeolite-A ion-exchanged with silver, copper, and zinc against a broad range of microorganisms, Appl. Biochem. Biotechnol. 172 (2014) 1652–1662, https://doi.org/10.1007/s12010-013-0647-7.

[48] F. Bakkali, S. Averbeck, D. Averbeck, M. Idaomar, Biological effects of essential oils - a review, Food Chem. Toxicol. 46 (2008) 446–475, https://doi.org/10.1016/j.fct.2007.09.106.

[49] L. Motelica, B.S. Vasile, A. Ficai, A.V. Surdu, D. Ficai, O.C. Oprea, E. Andronescu, G. Mustățea, E.L. Ungureanu, A.A. Dobre, Antibacterial activity of zinc oxide nanoparticles loaded with essential oils, Pharmaceutics 15 (2023), https://doi.org/10.3390/pharmaceutics15102470.

[50] Y. Shi, J. Shen, D. Yang, J. Du, S. Lu, M. Ma, H. He, S. Chen, X. Wang, Green cinnamaldehyde and thymol modified zinc oxide with double synergistic antibacterial effects in polypropylene, J. Appl. Polym. Sci. 138 (2021), https://doi.org/10.1002/app.50911.

[51] L. Motelica, D. Ficai, O. Oprea, A. Ficai, R.D. Trusca, E. Andronescu, A.M. Holban, Biodegradable alginate films with ZnO nanoparticles and citronella essential oil-a novel antimicrobial structure, Pharmaceutics 13 (2021), https://doi.org/10.3390/pharmaceutics13071020.